RESEARCH ARTICLE

Stefano Tinti · Gianluca Pagnoni · Filippo Zaniboni

The landslides and tsunamis of the 30th of December 2002 in Stromboli analysed through numerical simulations

Abstract On the 30th of December 2002 two tsunamis were generated only 7 min apart in Stromboli, southern Tyrrhenian Sea, Italy. They represented the peak of a volcanic crisis that started 2 days before with a large emission of lava flows from a lateral vent that opened some hundreds of meters below the summit craters. Both tsunamis were produced by landslides that detached from the Sciara del Fuoco. This is a morphological scar and is the result of the last collapse of the northwestern flank of the volcanic edifice, that occurred less than 5 ka B.P. The first tsunami was due to a submarine mass movement that started very close to the coastline and that involved about 20×10^6 m³ of material. The second tsunami was engendered by a subaerial landslide that detached at about 500 m above sea level and that involved a volume estimated at $4–9 \times 10^6$ m³. The latter landslide can be seen as the retrogressive continuation of the first failure. The tsunamis were not perceived as distinct events by most people. They attacked all the coasts of Stromboli within a few minutes and arrived at the neighbouring island of Panarea, 20 km SSW of Stromboli, in less than 5 min. The tsunamis caused severe damage at Stromboli.

In this work, the two tsunamis are studied by means of numerical simulations that use two distinct models, one for the landslides and one for the water waves. The motion of the sliding bodies is computed by means of a Lagrangian approach that partitions the mass into a set of blocks: we use both one-dimensional and two-dimensional schemes. The landslide model calculates the instantaneous rate of the vertical displacement of the sea surface caused by the motion of the underwater slide. This is included in the governing equations of the tsunami, which are solved by means of a finite-element (FE) technique. The tsunami is computed on two different grids formed by triangular elements, one covering the near-field around Stromboli and the other also including the island of Panarea.

The simulations show that the main tsunamigenic potential of the slides is restricted to the first tens of seconds of their motion when they interact with the shallow-water coastal area, and that it diminishes drastically in deep water. The simulations explain how the tsunamis that are generated in the Sciara del Fuoco area, are able to attack the entire coastline of Stromboli with larger effects on the northern coast than on the southern. Strong refraction and bending of the tsunami fronts is due to the large near-shore bathymetric gradient, which is also responsible for the trapping of the waves and for the persistence of the oscillations. Further, the first tsunami produces large waves and runup heights comparable with the observations. The simulated second tsunami is only slightly smaller, though it was induced by a mass that is approximately one third of the first. The arrival of the first tsunami is negative, in accordance with most eyewitness reports. Conversely, the leading wave of the second tsunami is positive.

S. Tinti (✉) · G. Pagnoni · F. Zaniboni
Dipartimento di Fisica, Settore di Geofisica, Università di Bologna,
Bologna,
Viale C. Berti Pichat,
8-40127 Bologna, Italy
e-mail: steve@ibogfs.df.unibo.it
Tel.: +39-051-2095025
Fax: +39-051-2095058

Introduction

The volcanic island of Stromboli belongs to the Aeolian group in the southern Tyrrhenian Sea, Italy. The volcano is characterized by persistent Strombolian activity, consisting of periodic explosions from the summit vents every 10–20 min, and of more intense eruptions with the rate of few occurrences per year. Sporadically, much stronger eruptions take place and may manifest with ejection of

scoria and bombs impacting over a very large area around the cone. They are characterized by eruption columns, ash clouds, pyroclastic flows, large lava flows from the main or from new ephemeral vents and by the occurrence of cracks and collapses. Several of such paroxysms occurred in the last century, and some of them were accompanied by tsunamis (for a detailed compilation, see the tsunami catalogue by Tinti et al. (2004), and the recent re-examination of the Aeolian tsunamis by Maramai et al. 2005). The last of such a crises lasted from December 2002 until July 2003, and forced the civil protection authorities to order the evacuation of the island for some months. On the 28th of December 2002, a big fissure opened at the base of the northeastern crater of the volcano and abundant lava flows spread on the northern part of the Sciara del Fuoco down to the sea. On December 30, at about 11:30 local time (GMT+1), a helicopter-borne survey revealed that smokes and vapours were rising from a very long fracture on the Sciara del Fuoco slope (Bonaccorso et al. 2003), which was interpreted a posteriori as the upper crown and the lateral flanks of the subaerial portion of the landslide.

The main episodes of failures occurred 2 h later, at 13:15 and at 13:22 local time. They were recorded by short-period and broadband seismometer stations located in Stromboli and in Panarea, an island located some 20 km SSW of Stromboli (see map in Fig. 1). The analysis of the records allowed the starting time of the mass movements to be determined and the conclusion to be drawn that they were complex processes involving several episodes of failure. Notice, however, that the identification of each sliding episode and the corresponding volume is rather difficult and uncertain (Bonaccorso et al. 2003; Pino et al. 2004; La Rocca et al. 2004).

Both landslides caused a tsunami. The tsunamis were recorded by a tide-gauge that was installed at Panarea jointly by INGV-CNT and by ISMAR-CNR to monitor

processes of anomalous submarine gas-emission and sea-floor deformations that were occurring a few kilometres off the coast of Panarea. The instrument was set to record the sea level averaged over a time window of 40 s at time steps of 5 min and was placed only 40 cm below the lowest expected tide. Therefore, the record is useless for precisely distinguishing and determining the arrival times of the two tsunamis, and is also strongly biased due to the cut of the negative waves below the threshold. Because of the insufficiency of the instrumental data, the reports of the eyewitnesses collected soon after the disaster are pivotal for reconstructing the sequence of the events (Tinti et al. 2005a). From their analysis, it was concluded that two distinct tsunamis were generated, and that probably they were both large enough to be destructive in Stromboli. They attacked various segments of the coast with different levels of violence, and, in most places, the second was probably weaker than the first one.

This work focuses on the numerical simulations of the events. A code consisting of two distinct models is used to simulate the motion of the landslides and the propagation of the ensuing tsunamis. For the sake of clarity, the paper is structured according to the topics rather than to the chronological sequence of the facts. Therefore, we treat the modelling of both landslides in the next section, and devote the subsequent one to the simulations of the tsunamis. The discussion of the results forms the conclusive section of the paper.

The landslides

The landslides left very distinct signals on seismograms recorded by short-period, intermediate-period and broad-band seismometer stations, managed by different sections of INGV (i.e. INGV-CT, INGV-OV and INGV-CNT). Their analysis shows that the onset of the first mass movement can be estimated to have occurred at around 13:14–13:15 local time, and the beginning of the second at 13:23 local time (Bonaccorso et al. 2003; Pino et al. 2004; La Rocca et al. 2004). Both signals can be interpreted as the effect of multiple impulses, suggesting that failures occurred in various steps and that the process was quite complex. Surveys conducted in the following days permitted us to ascertain a relevant mass defect along the slope of the Sciara del Fuoco, both above and below the sea level. The dynamics of the mountain flank due to the ongoing eruption (lava flows, progressive failures and demolition of unstable spurs and slopes) remained intense for several days, and made it difficult to provide an accurate estimation of the geometry and the volumes of the tsunamigenic landslides. Aerophotogrammetric data taken in May 2001 as well as few days after these events, show that the volume missing from the northern side of the Sciara del Fuoco was in the range of 10^7 m^3 above sea level (Baldi et al. 2003). Bathymetric surveys off Sciara del Fuoco revealed a deep underwater signature continuing the subaerial scar, suggesting a mobilized volume in the order of 20×10^6 m^3 (Chiocci et al. 2003).
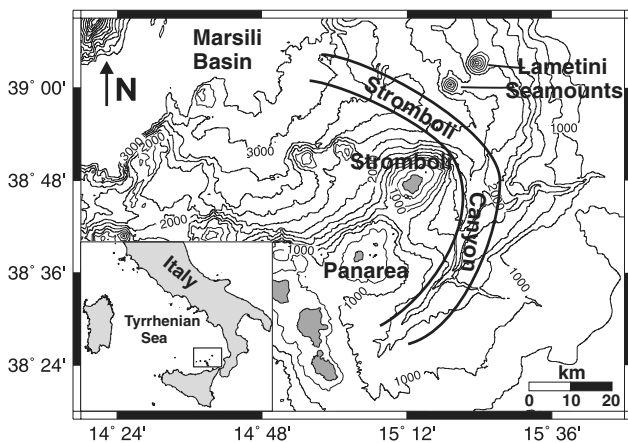

Fig. 1 Geographic map of the Tyrrhenian Sea around the island of Stromboli. Panarea is the closest inhabited island of the Aeolian group, about 20 km to SSW. More to the south, there are the other islands of the Aeolian group. To the north one finds the Lametini seamounts separated from Stromboli by the deep Stromboli Canyon ending in the abyssal plain (Marsili basin), deeper than 3200 m

From the account of an eyewitness who was observing what was happening from a point located in the southern margin of the Sciara del Fuoco, we know that the first mass movement was submarine. The witness saw the sea open suddenly close to the shore, uncovering the bottom (he described it as a sudden cut in the water), and then recede from the shoreline. He also saw the occurrence of the second tsunamigenic landslide, which he described as the sliding motion of a single entity entering the sea, which took place a short time (he was not able to specify better) after the first tsunami (Tinti et al. 2005a).

Modelling the motion of landslides is not a simple task and is still an open topic of research. The processes leading up to a mass becoming unstable and its post-failure dynamics are very complex and depend on a large number of factors that are often difficult to quantify correctly such as the rheology and the geotechnical properties of the materials involved. Numerical techniques may describe the mass as a set of interacting particles or as a dense granular flow (Louge and Keast 2001; Pitman et al. 2003), a viscous fluid, or may even use the concept of cellular automata (Dattilo and Spezzano 2003). Here, we use a model based on the discretization of the mass into a set of blocks that are allowed to deform, but not to change volume during the motion. The model uses a Lagrangian point of view rather than an Eulerian approach, since the former is more suitable for describing the dynamics of masses like mobile objects or sliding bodies where translation is the main feature (Chen and Lee 2003). The code was originally conceived in a simplified one-dimensional version (Tinti et al. 1997) and then enhanced to a two-dimensional model. The sliding body is partitioned into a chain of blocks (one-dimensional) or into a matrix of blocks (two-dimensional). The model computes the motion of the centre of mass (CoM) of the constituent blocks. The acceleration of the CoM of the block j at the time t_i can be given the expression:

$$\vec{\mathbf{a}}_{ij} = \vec{\mathbf{G}}_{ij} + \vec{\mathbf{R}}_{ij} + \vec{\mathbf{F}}_{ij}$$

Here $\vec{G}_{ij}$ is the sum of two terms and has the form:

$$\vec{\mathbf{G}}_{ij} = \rho^*(g \, \sin \, \vartheta'_{ij} \vec{\mathbf{n}}_{ij} - \mu \, \cos \, \vartheta_{ij} \vec{\mathbf{m}}_{ij})$$

where ρ^* is the reduced density, i.e.:

$$\rho^* = \frac{(\rho' - \rho)}{\rho'}$$

with $\rho\prime$ and ρ we denote respectively the density of the sliding mass and of the ambient fluid, which is taken to be equal to zero in the case of subaerial slides. The first term is the driving gravity acceleration, the second is the basal friction term proportional to the friction coefficient μ. These terms depend on the local relief slope ϑ'_{ij} and ϑ_{ij}, that are taken respectively along the direction of the unit vectors $\vec{\mathbf{n}}_{ij}$ and $\vec{\mathbf{m}}_{ij}$, the former being aligned with the topographical gradient, the second with the block velocity vector.

The term $\vec{\mathbf{R}}_{ij}$ is the resistance term opposing the motion and acting on the overall surface of the block that is in contact with the ambient fluid. It depends on the square of the relative velocity of the block with respect to the fluid, and it is here approximated with the square of the velocity of the block. It is overlooked for subaerial slides, but plays an important role for the submarine ones. It may be given the expression:

$$\vec{\mathbf{R}}_{ij} = \vec{\mathbf{R}}_{ij}^{\text{sup}} + \vec{\mathbf{R}}_{ij}^{\text{exp}}$$

where the resistance is split into the contributions due to the upper surface of the block ($\vec{\mathbf{R}}_{ij}^{\text{sup}}$) and to the portions of the lateral surfaces that are exposed, i.e. that face the impact of the fluid and are not masked by the adjacent blocks ($\vec{\mathbf{R}}_{ij}^{\text{exp}}$).

The former has the form:

$$\vec{\mathbf{R}}_{ij}^{\text{sup}} = \frac{\rho' C_d}{2\rho H_{L,ij}} \vec{\mathbf{v}}_{ij} |\vec{\mathbf{v}}_{ij}|$$

where $H_{L,ij}$ is the instantaneous height of the block j, and $\vec{\mathbf{v}}_{ij}$ is its velocity. The latter ($\vec{\mathbf{R}}_{ij}^{\text{exp}}$) results from the sum of the resistance on all the N_j side faces that form the instantaneous front of the block j at a given time. If $\vec{\mathbf{v}}'_{ijk}$ is the mean velocity of the face k of the block j, and $A_{ijk}^{\text{exp}} \vec{\mathbf{l}}_{ijk}$ is the corresponding exposed surface ($\vec{\mathbf{l}}_{ijk}$ being an outward unit normal vector), then the instantaneous frontal faces are those for which the scalar product $\vec{\mathbf{v}}'_{ijk} \cdot \vec{\mathbf{l}}_{ijk}$ is greater than zero. Hence, this term can be written as:

$$\vec{\mathbf{R}}_{ij}^{\text{exp}} = \sum_{k=1}^{N_j} \frac{\rho' C_f A_{ijk}^{\text{exp}}}{2\rho V_j} |\vec{\mathbf{v}}'_{ijk}| \max(\vec{\mathbf{v}}'_{ijk} \cdot \vec{\mathbf{l}}_{ijk}, 0)$$

Notice that the speed of the CoM $\vec{\mathbf{v}}_{ij}$ and of the lateral surfaces of the block $\vec{\mathbf{v}}'_{ijk}$ may differ from each other and must be computed separately by the code. In the numerical experiments of this paper, the coefficients C_d and C_f in the above expressions are taken to be zero as the mass moves outside the water, while underwater they are given the respective values 0.01 and 2.0 for both one-dimensional and two-dimensional simulations. These values are typical for submarine slides, as demonstrated e.g. by the sensitivity study undertaken for the Holocene Stromboli lateral collapse by Tinti et al. (2000).

The term $\vec{\mathbf{F}}_{ij}$ is the contribution of the internal forces and is the sum of the interactions of block j with the others. It can be written as (see Tinti et al. 1999 for the one-dimensional formulation, and Bortolucci 2001 for the two-dimensional implementation):

$$\vec{\mathbf{F}}_{ij} = \frac{1}{M \Delta t} \sum_{k \neq j} \beta_{ijk} m_j (1 - e_{ijk})(\vec{\mathbf{v}}_{ij} - \vec{\mathbf{v}}_{ik})$$

Here Δt is the computation time step, M is the total mass of the body, m_j is the mass of the j-th block, e_{ijk} is the instan-

taneous interaction coefficient between blocks j and k, and β_{ijk} is a function of the effective interaction length. This function equals 1 below the minimum inter-block interaction distance $d_{\min}$ and zero above the maximum interaction distance $d_{\max}$, because it varies linearly from 1 to 0 in the intermediate range $(d_{\min}, d_{\max,})$. The above summation is formally extended to all the blocks of the slide but block j. However, the actual number of the blocks interacting with block j is regulated by means of the function β_{ijk}, depending on the instantaneous distance of the CoMs of blocks j and k. In typical implementations, the parameters $d_{\min}$ and $d_{\max}$ are such that block j interacts predominantly with the next blocks. The interaction coefficients e_{ijk} express the level and type of interaction between block j and block k, and depend on the deformation history of the body. The parameters used in the expression of these coefficients are the intensity coefficient $\bar{\lambda}$, the deformability coefficients σ and σ_1, and the shape coefficient γ, whose definitions are introduced and discussed in Tinti et al. (1997)for the one-dimensional model, remaining substantially unchanged in the two-dimensional implementation. For further details, the reader may refer to Bortolucci (2001) and to Zaniboni (2004). The values used in this paper for both one-dimensional and two-dimensional models are: $\bar{\lambda} = 0.05$, $\sigma = 0.2$, $\sigma_1 = 0.8$, $\gamma = 0.01$, and conform with the range of values used in previous works (e.g. Tinti et al. 2000).

In the one-dimensional model, all computations are restricted to the components of the block acceleration, velocity and displacement that are tangential to the prescribed common trajectory of the CoM, and, therefore, all the above vector expressions may be substituted by scalar ones. Conversely, in the two-dimensional model, the CoM trajectories are unknown and are calculated dynamically step by step. The only obvious constraint that is applied is that the CoMs are bound to belong to the prescribed sliding surface. The parallel between one-dimensional and two-dimensional computations may be described, for example, by considering the expression of $\vec{G}_{ij}$ that was given explicitly above. The unit vector $\vec{m}_{ij}$ in the expression of the bottom friction is parallel to the instantaneous block velocity, and, consequently, lies along the block trajectory in both the one-dimensional and two-dimensional models. On the other hand, the meaning of the unit vector $\vec{n}_{ij}$ differs in the two models. In the two-dimensional approach, $\vec{n}_{ij}$ is in the direction of the local maximum topographical (or bathymetric) gradient, and ϑ'_{ij} is the corresponding slope. Instead, in one-dimensional $\vec{\vec{n}}_{ij}$ is identical to $\vec{m}_{ij}$, being tangent to the block trajectory, and hence ϑ'_{ij} identifies with ϑ_{ij}, i.e. the local slope that is measured along the common path of all the blocks.

The simulation of the landslides

Several landslide simulations have been run, but we describe here only the results of four cases that we consider the most relevant ones: two runs for the first submarine landslides (denoted here case 1A and case 1B), one run for the second subaerial landslide (case 2), and one run for a hypothetical landslide that has both a submarine and a subaerial volume (case 3). The aspect ratio of the first landslide, i.e. the ratio of transversal width over longitudinal length, is about one third; hence the motion of the first landslide is properly modelled by means of the two-dimensional model. The volume (about 16 million m^3) and the initial underwater position are the same for both cases 1A and 1B and may be seen in Fig. 2. The position corresponds to the place of the submarine scar observed by post-event bathymetric surveys and covers an area about 700 m wide and 2.2 km long down to 750 m below sea level (Chiocci et al. 2003). Cases 1A and 1B differ as regards the mass distribution of the sliding body. In case 1A, the body has a simple triangular transversal section, axially symmetric, with uniform thickness downslope. Case 1B corresponds to a body with unequal mass distribution downhill: the slide thickness is higher in the near-shore region (about 35 m) and diminishes gradually offshore, which conforms better to experimental data. A three-dimensional view of the initial shape hypothesized for the slides is portrayed in Fig. 3. The bodies are discretized into a matrix of blocks with quadrilateral basal area. The number of blocks is purposely kept small (15 for case 1A and 32 for case 1B). This allows only a gross description of the body, which is however sufficiently accurate to permit the computation of the excited tsunami, since tsunamigenic potential is rather insensible to space and time high-frequency details.

Cases 2 and 3 are treated by means of the simplified one-dimensional model, which is enough to provide the resolution required, given the narrowness of the body mass cross-section in the uphill part of the slide: for example, for case 2, the aspect ratio is as small as about one sixth. The initial footprint of the slides of case 2 and case 3 is sketched in Fig. 2. The subaerial slide occupies the northern sector of the Sciara del Fuoco reaching the coastline. It corresponds to the area in which a double scar was observed on the morning of the 31st of December during a helicopter-borne photographic survey (Bonaccorso et al. 2003). The volume considered here is less than 5×10^6 m^3, accounting for about 50% of the missing mass as evaluated by comparing pre-crisis and post-event photogrammetric data (Baldi et al. 2003). Case 3 is presented to complete the discussion. It deals with a slide that initially is partly submerged and partly above the sea level, possessing a volume about the same magnitude as cases 1 and 2. However, it is believed that it represents neither the first nor the second landslide. As already mentioned, the one-dimensional model requires that the common trajectory of the slide blocks is prescribed, together with the portion of the sliding surface that is swept by the body. For cases 2 and 3, Fig. 2 shows the trajectory we impose on the CoM of the blocks, and also the specified lateral boundaries of the swept surface of sliding. The trajectory has been selected based on the results of the two-dimensional simulations that were run for cases 1A and 1B, and follows approximately a line of maximum topographic gradient.
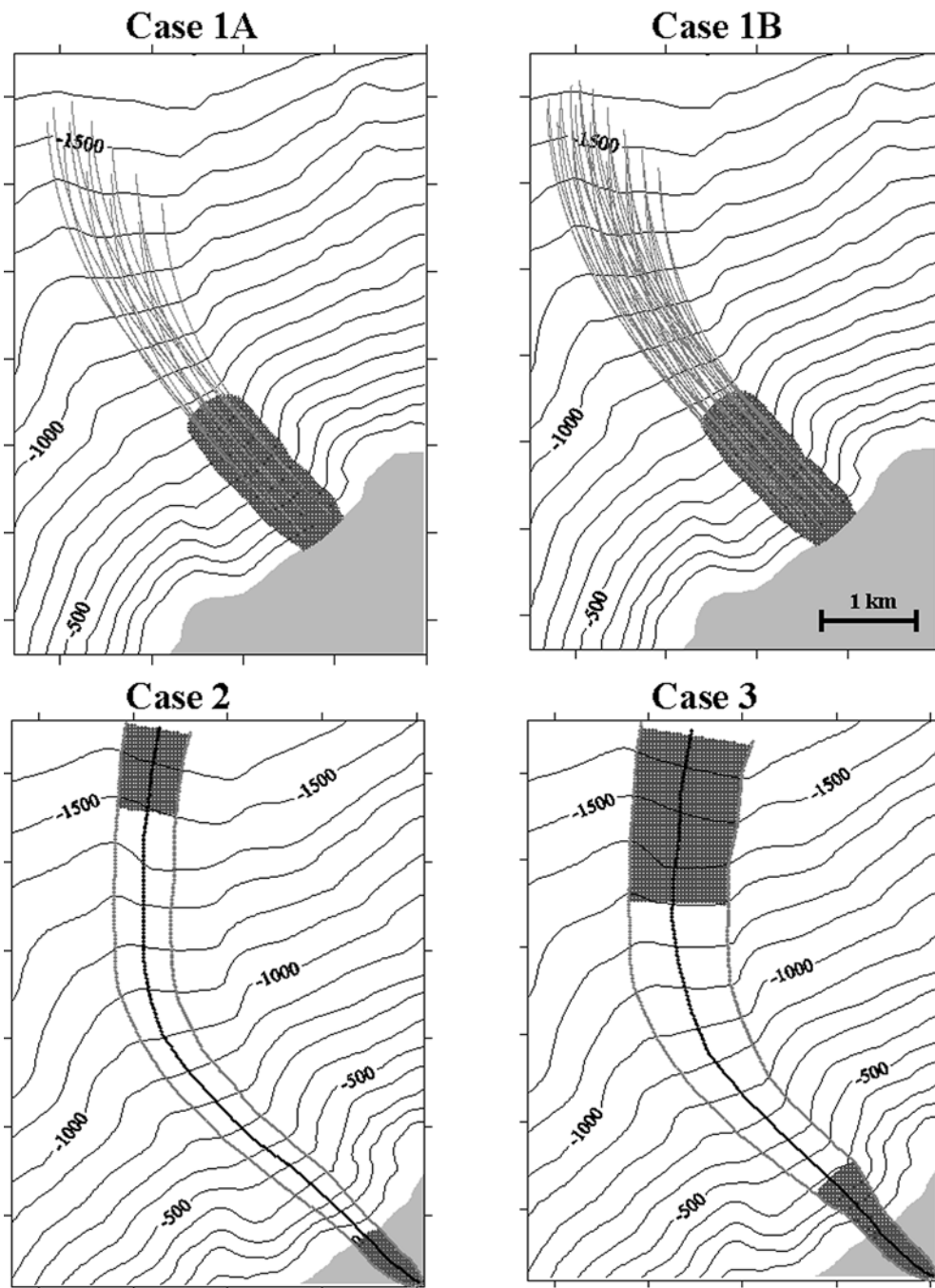
Case 1A

Case 1B

Case 2

Case 3

Fig. 2 Two-dimensional view of the motion of the landslides in the sea region in front of the Sciara del Fuoco. Case 1B and case 2 represent the first and the second tsunamigenic landslides, respectively. Cases 1A and 1B have the same initial footprint and initial mass, but different mass distribution. They have been treated with the two-dimensional landslide model. The trajectories of the blocks forming the slide (*grey lines*) are computed via the model. Cases 2 and 3 have been treated through the one-dimensional model requiring the specification of the trajectory of the CoM (*black line*) and of the lateral boundaries of the sliding surface (*grey lines*). The position of the landslides at the beginning and at the end of the computation are portrayed in *dark grey*. Bathymetric labels are in m

The motion of the slides is calculated within a region that is only slightly larger than the area included in the map of Fig. 2, down to a sea depth of about 1,800 m. In fact, as will be remarked in the next section, the tsunamigenic potential of these moving bodies diminishes rapidly with the sea depth. The trajectories of the blocks composing the mass in the two-dimensional simulations are plotted in

Fig. 2 up to 120 s for case 1A and about 150 s for case 1B. These are calculated dynamically by the numerical code. The change in shape of the body during sliding is reflected by the fact that block trajectories depart, cross each other and spread. At later computation times, the slides exit from the map. In cases 2 and 3, the body is constrained to sweep a predefined sliding surface. The positions of the slides
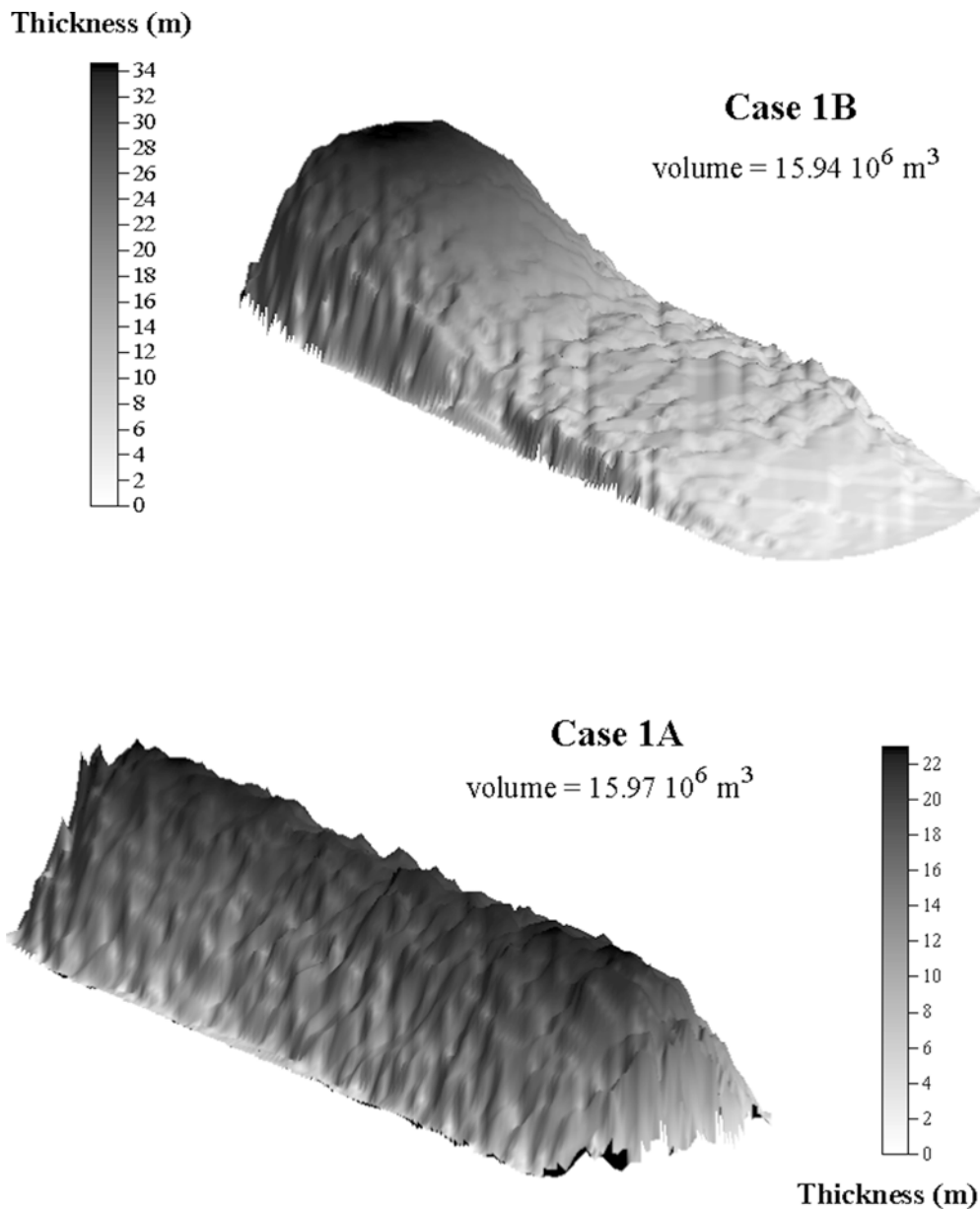
Thickness (m)

Case 1B

volume = $15.94 \ 10^6 \ m^3$

Case 1A

volume = $15.97 \ 10^6 \ m^3$

Thickness (m)

Fig. 3 Three-dimensional view of the submarine slides. Case 1A has a triangular cross-section and is uniform in the longitudinal direction. Case 1B has an almost uniform cross-section and a very unequal longitudinal distribution: maximum thickness near-shore and almost linear decay seaward

close to the northern side of the mapped area are shown in Fig. 2; they are attained respectively after about 180 s and after 153 s. The resulting magnitude of the velocity of the blocks is graphed in Fig. 4 vs. time. It may be seen that in all cases the motion is characterized by a first phase of strong acceleration followed by a long phase of weaker deceleration. The main, but not unique, factor governing the acceleration is the local slope of the sliding surface. Cases 1A and 1B deal with slides with the same initial position, and therefore the initial phase of their motion is very similar, being mainly dictated by the same values of the driving gravity acceleration. Later, the motion of the two slides differentiates basically because the body of case 1B is thicker near-shore, and is affected by a stronger resistive drag. The

subaerial slide (case 2) starts on a steeper incline and hence gains large velocities more quickly. The academic case 3 is intermediate between the pair of cases 1A–1B and case 2 as regards the initial position, and therefore it is not surprising that the computed block velocities of the first phase of the motion are found to lie in between (see Fig. 4). The computed peak velocities are high, ranging from 30–60 m/s, but are lower than the largest estimates that can be found in the literature for open-air landslides collapsing into the sea (see Ward and Day 2002). The velocity plot stops when block velocities are still rather large, which means that the slides are still far from their final position. The slide deposits are expected to be in much deeper ocean, possibly in the sector of the Stromboli canyon deeper than 2,500 m, west to the
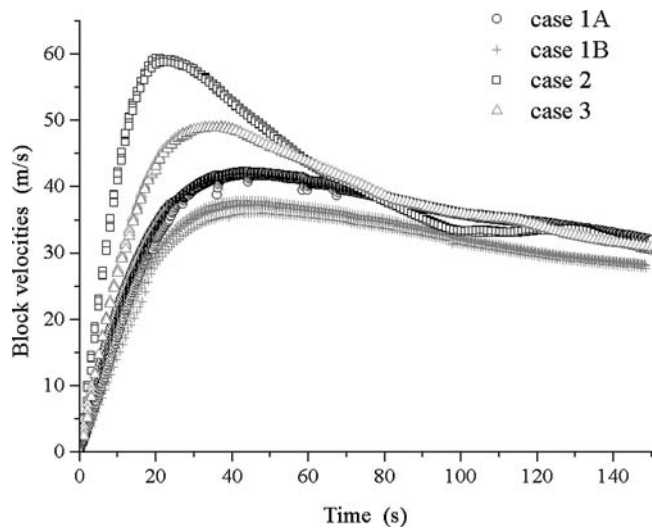
Fig. 4 Velocities of the blocks forming the landslides vs. time. Different symbols are used for different cases. At a given time, the velocities of the blocks composing the same landslide usually differ from each other: the more they depart, the larger are the spread of the symbols and the apparent thickness of the plotted curve. The subaerial slide (case 2) attains the peak speed in about 20 s (it starts on a steeper slope with no ambient fluid resistance), whereas the submarine slide (case 1B) is the slowest one at any time and is the last to reach its maximum speed. For graphical purposes, only a subset of symbols is plotted

Lametini seamounts and close to the Marsili basin in the abyssal Tyrrhenian plain (Fig. 1); this is believed to correspond to the place where sediments from failures of the Stromboli flanks are mostly transported (Kidd et al. 1998; Scherreiks 2000).

The landslide simulation code allows for the computation of the Froude number *Fr* that plays a relevant role in tsunami generation by submarine landslides (Tinti and Bortolucci 2000a,b). For a rigid body, sliding underwater on a flat-bottom ocean of depth *h*, *Fr* is defined as the ratio of the horizontal velocity of the body V_h to the celerity of the water waves, that in shallow water approximation is simply $(gh)^{1/2}$, i.e. $Fr = V_h/(gh)^{1/2}$. More generally, for a deformable body sliding over a more complex bathymetry, the *Fr* may be defined and computed as the average taken over the submerged portion of the body of the local Froude numbers. For a slide partitioned into blocks, it is straightforward to calculate the average Froude number of the slide by extending the summation to all underwater blocks. The results are shown in Fig. 5a and b, where the average Froude numbers are plotted as a function of time for the four cases considered here. It is seen that all curves have an initial growth and a subsequent decrease. In the initial stage, both numerator and denominator of the Froude number ratio increase, but the weight of speed gain (numerator) prevails on the effect of depth increase (denominator). In the second phase, the body slows down and advances toward larger depths, and these are factors both accounting for the reduction of *Fr*. The curves corresponding to cases 1A and 1B, i.e. to slides that move from an initial under-
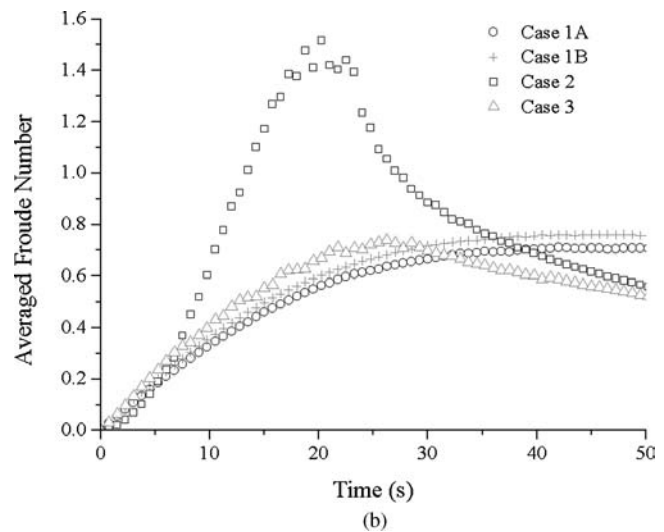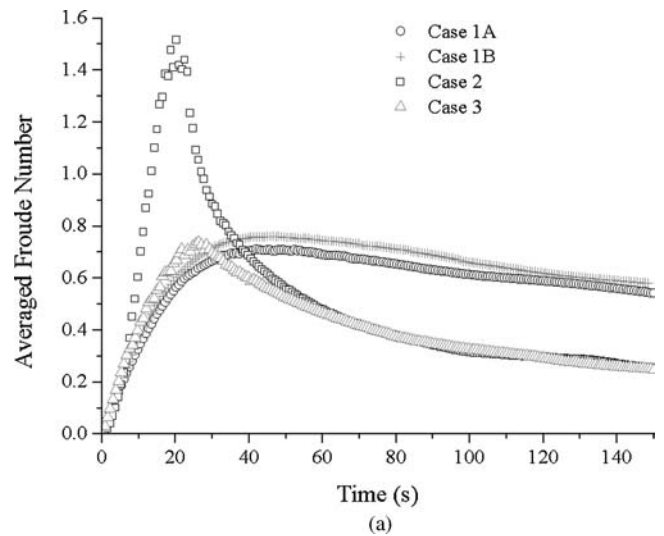

Fig. 5 Average Froude numbers vs. time in the first 150 s of motion (**a**); zoomed in the first 50 s-long interval of time (**b**). The slide Froude number is computed through a weighted average taken over the blocks forming the slide, the weight being the volume of the blocks. Notice that the subaerial slide (case 2) is the only one attaining values larger than 1: it crosses the critical line *Fr*=1 twice. In shallow-water theory, slides moving at the critical regime (*Fr* = 1) are the most effective in generating tsunamis. Only a subset of symbols is plotted

water position, are quite smooth and close to one another, remaining always below the value of 1. Curve 2 regards the subaerial mass. At the beginning, when the slide enters the sea, its rate of change is quite large, and its peak value is far greater than unity. Later, it quickly attains values smaller than the previous cases 1A and 1B. This is due to the fact that in the range of times 80–150 s, these slides have yet similar speeds, but the slide of case 2 has reached a much larger depth, since it was much faster in the initial phase. Curve 3 concerns the case of the slide partially submarine and partially subaerial. A net change of gradient may be observed in the curve slightly after 25 s, which is the time

when all the subaerial volume of the slide ends entering the sea water.

The tsunamis

Tsunamis generated by landslides have recently gained a lot of interest in the last decade with the consequences of several events severely hitting coastal communities worldwide. This mechanism was overlooked in the past when the attention was predominantly addressed to tsunamis of tectonic origin. A critical reanalysis of the historical compilations shows that the rate of tsunamis caused by mass movements is higher than it was thought in the Pacific (Gusiakov 2001), and probably this is also true for other seas and oceans in the world.

Numerical models of landslide-induced tsunamis can be basically split into two main categories. One class treats the slide and the water as a two-phase fluid and computes the motion of the two phases by simultaneously solving the set of the coupled fluid mechanics equations, accounting for the full water-slide interaction. This approach is intrinsically more convenient for describing the motion of viscous mudslides or dense turbidity currents (Jiang and Leblond 1992, 1994), though examples of application to tsunamigenic slumping can be found in the literature (Hebert et al. 2002; Rabinovich et al. 2003). The second class of models computes the tsunami by providing the motion of the sea bottom as a known input to the hydrodynamic model. The main concept is that the underwater movement of the slide determines the change of the local sea depth with time, which is considered the most important factor for tsunami generation. In some of these models the motion of the landslide is assumed to be quite elementary, such as the one of a rigid body sliding down a frictional incline (Harbitz 1992; Watts 2000). Our approach may be classed in this second category, but in our case, the motion of the sliding mass is computed in a more sophisticated way by means of the Lagrangian model described in the previous section.

The set of hydrodynamics equations governing the water motion derive from the non-linear non-dispersive Navier-Stokes theory applied to a fluid with depth-averaged particle velocity, and may be written as:

$$\partial_t \eta = \partial_t h_s - \nabla \cdot [(h + \eta)\vec{\mathbf{v}}]$$

$$\partial_t \vec{\mathbf{v}} = -g \nabla \eta - \left(\vec{\mathbf{v}} \cdot \nabla \vec{\mathbf{v}}\right)$$

The first equation is the continuity equation, while the second expresses the conservation of the momentum. Here η is the water elevation above the still water level, h is the local ocean depth and $\vec{\mathbf{v}}$ is the depth-averaged horizontal velocity vector, while g is the gravity acceleration. On the open boundary of the computational domain, the condition imposed is:

$$\vec{\mathbf{v}} \cdot \vec{\mathbf{n}} = \frac{g}{c} \eta$$

which allows the tsunami to cross the boundary of the domain with no undesired back-reflection. Here $\vec{\mathbf{n}}$ denotes the unit vector pointing outward. On the coastal boundary the condition is:

$$\vec{\mathbf{v}} \cdot \vec{\mathbf{n}} = \frac{g}{c} \eta (1 - R)$$

where R is the coastal reflection coefficient, falling in the interval (0, 1). The condition $R=1$ corresponds to a pure reflection of the wave against the coast, while the boundary is partly translucent if $R<1$, implying that energy is lost in the interaction with the boundary. A further observation is that the model assumes that the shoreline is stationary and does not move with water waves, which is equivalent to assuming that the boundary is a vertical wall. Technically, this does not permit the computation of water flooding and water runup heights, but only the maximum water elevation at the coast. This is not a serious limitation, since it is known that the maximum water elevation is a good approximation of the runup heights, and departures can occur in the presence of special local conditions (i.e. positive interference of fronts, coastal morphology favouring confluence and transient piling up of incoming water masses, etc.). An additional loss of energy can be imposed at the coastal boundary, depending on the velocity component that is tangent to the coast, i.e.:

$$\partial_t K \propto -(\vec{\mathbf{v}} \cdot \vec{\mathbf{t}})^2 (1 - C_t^2)$$

Here K denotes the density per unit area of the kinetic energy of the tsunami, $\vec{\mathbf{t}}$ is the unit tangent vector and C_t is a coefficient in the interval (0, 1). When $C_t=1$, the boundary is frictionless and no energy is lost, whereas in case of $C_t=0$, the dissipation of energy due to currents parallel to the coast is maximum.

In all our computations, we assumed $R=0.99$ and $C_t=0.95$, which has the double effect of (1) controlling the onset of numerical instabilities that may appear in the long run in proximity of boundary strong irregularities, and (2) causing a modest energy loss at the coastal boundaries. This second feature is practically equivalent to the energy dissipation that could be numerically obtained by adding the more traditional bottom friction term $-C_b \vec{\mathbf{v}} |\vec{\mathbf{v}}| (h + \eta)^{-1}$ on the r.h.s. of the momentum equations given above, where the bottom friction coefficient C_b is taken either to be constant (see e.g. Mader 1988 ; Satake 1995; Tinti et al. 2000), or dependent on the total water depth through the Manning's roughness coefficient (see e.g. Choi et al. 2003).

The term $\partial_t h_s$ in the continuity equation is the tsunami generation term, and is the link between the landslide model and the tsunami model. h_s denotes the instantaneous sea surface elevation caused by the transit of the underwater landslide. In our model, the relation between h_s and the local thickness H_L of the slide at the sea bottom (computed by the landslide simulation code) is calculated by means of a transfer function that depends on the local ocean depth h, according to the law:

$$\partial_t h_s = \partial_t H_L \operatorname{sech} \alpha, \quad \alpha = \frac{2\pi h}{L_S}$$

where L_S is the characteristic length of the underwater portion of the slide. This function filters out the high-frequency signals, in agreement with the theoretical formula of the Green's function of three-dimensional theory of water wave propagation (see Kajiura 1963 ; Ward 2001; Ward and Day 2003). It is important to observe that, if one supposes that $\partial_t h_s$ is exactly equal to $\partial_t H_L$, this is equivalent to assuming that disturbances at the sea bottom are reproduced unchanged at the sea surface, which is a good approximation only when the slide length is much larger than the water depth, as conjectured in pure shallow-water models. Using the transfer function $\operatorname{sech} \alpha$ attributes differential tsunamigenic potential to landslides of different characteristic length L_S (and correspondingly of different basal area) and moving at different ocean depth. One effect is that landslides have much more capability of exciting water waves when they move near-shore ($\alpha \approx 0$ and $\partial_t h_s \approx \partial_t H_L$) than when they run in very deep ocean $\alpha \gg 1$ (and $\partial_t h_s \ll \partial_t H_L$).

The excitation term $\partial_t h_s$ has to be provided as a known input to the tsunami simulation code over the nodes of the tsunami mesh at any time step, as long as the landslide is in motion. Since the two models make use of different space grids, an interpolation interface performs the required mapping from one mesh to the other. One of the results provided by this interface code is the transfer function $\operatorname{sech} \alpha$ computed at any instant of time on all the nodes of the tsunami simulation mesh covered by the slide body. Figure 6 shows the transfer function averaged over the slide area as a function of time for the four landslide simulations considered in the paper. Hereafter it will be denoted equivalently as average transfer function or as slide transfer function. This
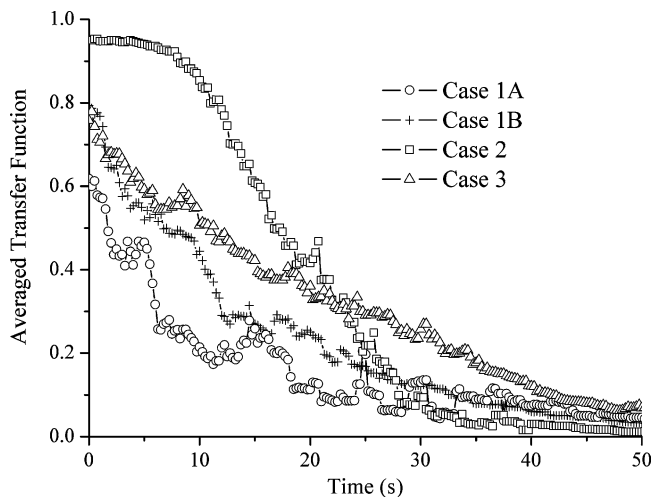

Fig. 6 Average transfer function $\operatorname{sech} \alpha$ vs. time. It is computed by taking the average of the function over all nodes of the tsunami simulation mesh that at a given time are covered by the slide. In the computation, the typical slide length L_S is taken as the square root of the basal area of the submerged portion of the slide that is provided by the landslide simulation code at each time step

average value is calculated and shown since it may help with the interpretation of the modelling results, but it is not used in the tsunami simulation code where it is computed distinctly in all nodes to provide the local excitation term of the continuity equation. All the average transfer functions in Fig. 6 have a decreasing trend and they attain very small values very quickly, since after only 40–50 s they are all as small as 0.1 or less. Further, the largest slide transfer function pertains to the subaerial slide simulation (case 2), at least in the initial 20-s-long time interval. Moreover, although the two slides 1A and 1B have exactly the same initial footprint, they exhibit quite different slide transfer functions as a consequence of the different mass distribution. Indeed, case 1B has more mass concentration in the shallow coastal region, where the ratio α is smaller and $\operatorname{sech} \alpha$ is higher, which also implies that the mean value of the transfer function is larger.

The simulation of the tsunamis

The shallow-water equations have been solved by means of a finite-element (FE) technique over two grids composed of triangular elements of unequal size. The first is a high-resolution grid covering only the source region and the near-shore belt of Stromboli: the complex geometry of the coastline is reproduced in a very accurate way in this grid. The second grid covers a larger geographical area including also the island of Panarea. The tsunamis were observed also outside this area, in the whole southern Tyrrhenian Sea, but their effects were negligible there compared to the impact in the region we have considered. The extension of these domains may be seen in Figs. 7 and 12 and in Figs. 11 and 15, where the calculated elevation fields of the tsunami associated with cases 1B and 2 are shown and that will be discussed later. The first grid, denoted hereafter as G1, is formed by 24,323 triangles corresponding to 12,612 nodes. The median of the distribution of the typical length L_T of the triangles (L_T is here defined as the square root of the area of the triangle) is about 64 m, and the first quartile of the L_T distribution is 8 m. The second grid, G2, is coarser, covering a larger area made up of a smaller number of elements. It includes 6,118 nodes and 11,735 triangles: 50% of the L_T values is below 440 m, while 25% is less than 240 m.

Only two tsunami simulations will be illustrated here in detail. These correspond to the landslide cases 1B and 2 that represent the first and second main landslide occurrences in our view. The tsunamis resulting from the remaining cases 1A and 3 will be only given a succinct description. The results of the simulation of the first tsunami (case 1B: submarine slide with irregularly distributed mass) are shown in the series of Figs. 7–11. The water elevation fields computed in grid G1 are portrayed in four different snapshots up to 150 s in Fig. 7. The tsunami nucleates from the source placed off Sciara del Fuoco and propagates seaward with almost circular fronts. The front travels much more slowly near the coast, and after 2.5 min since the landslide initiation, which coincides with the tsunami origin time, it has affected more than one half of the entire coastline of

Stromboli. Strong front bending occurs near-shore and is more accentuated along the southern coast, which is due to the steepness of the underwater slope of the volcanic edifice. As a consequence, an observer on the coast sees the tsunami front as advancing quickly offshore, and in certain places almost parallel to the coastline, and attacking the coast obliquely. The separation of the crests and troughs is much larger offshore than near-shore where the wave speed is low.

Figure 9 shows the mareograms calculated at a set of coastal nodes, that can be located on Stromboli with the aid of Fig. 8. The numbering for these points proceeds counterclockwise from a location that is named Malopasso (number 1) and is opposite to the source region. In Fig. 8, the star on the coast south of point 1 marks the origin from which the coastal distances are calculated. Points 2–8 correspond to the NE coastal segment from Pizzillo to Piscità that is the most densely inhabited by residents and tourists. Node 13 in the SW corner of the island corresponds to the little village of Ginostra located on a high cliff. The analysis of the tide-gauge records in Fig. 9 reveals that the main tsunami signal begins with a strong recession of the water (though it is sometime preceded by a quick small-amplitude water rise) and that the number of large waves changes from place to place. In the two nodes that are the nearest to the source area, one to the north (node 10) and the other to the south (node 11), the tsunami appears as a large-amplitude dipole wave (big trough-crest sequence) followed by a number of smaller oscillations. In more dis-
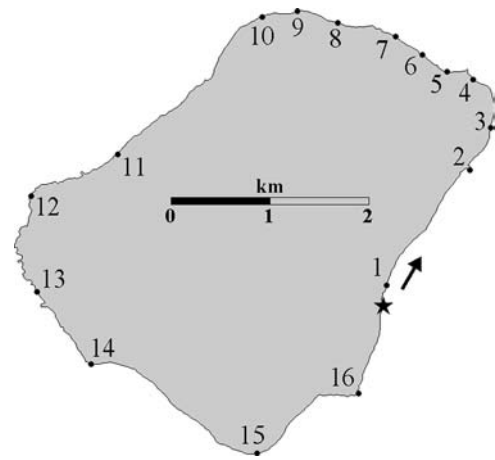

Fig. 8 Nodes of grid G1 located on the coastline of Stromboli. *Node 1* Malopasso, *Node 2* Pizzillo, *Node 3* Scari, *Nodes 4–5* Ficogrande, *Nodes 6–8* Piscità, *Node 9* Punta Frontone, *Node 10* Punta Labronzo, *Node 11* southern part of the Sciara del Fuoco, *Node 12* Punta Chiappe, *Node 13* Ginostra, *Node 14* Punta Lazzaro, *Node 15* (southern) Punta Lena, *Node 16* Punta dell'Omo. The (northern) Punta Lena is located between node 3 and node 4. The *star* shows the origin whence the along-coastal distance used in the following Figs. 10 and 11 is measured in the direction of the *arrow*

tant locations, the records are dominated by a number of two or three waves. The largest wave is not always the first one: it may be the second or the third one. Usually, the transition from negative to positive water elevation occurs more quickly than the inverse transition from crest to trough. This means that the shape of the travelling waves is strongly asymmetric and is characterized by steep fronts (like walls of water) that are probably close to breaking, a process that is not accounted for by the numerical model. Node 1, the one most distant from the source, is the last one to be attacked by the waves, and this takes places in less than 4 min. The main tsunami signal has a dominant period of about 1 min, though higher frequency oscillations may be seen corresponding especially to the large positive waves (e.g. see records no. 5, 6, 8, 9 and 12).

The maximum sea-level highs and lows computed along the entire coast of Stromboli (i.e. on all the coastal nodes of grid G1) are plotted in Fig. 10a. The graph shows clearly how the tsunami decays as the distance from the source increases. In the Sciara del Fuoco region, positive values of water elevation as large as 30–40 m are calculated, but on the opposite coast in most of the coastal segment from Punta Lazzaro (node 14) to Punta dell'Omo (node 16), the maximum elevation is less than 2 m. Figure 10b shows a detail of Fig. 10a. It zooms in on the coastline going from the south of Pizzillo (node 2) to Punta Frontone (node 9), located west of Piscità (node 8); in this piece of coast most of the structures of Stromboli vulnerable to the wave attacks are found, and here the damage caused by the tsunami was most severe. The maximum water elevations resulting from the model are compared to the runup heights measured in the field during several post-event surveys (Tinti et al. 2005b). The agreement is quite satisfactory, especially in the central part of the graph corresponding to the NE corner of Stromboli, from the northern Punta Lena (that lies between
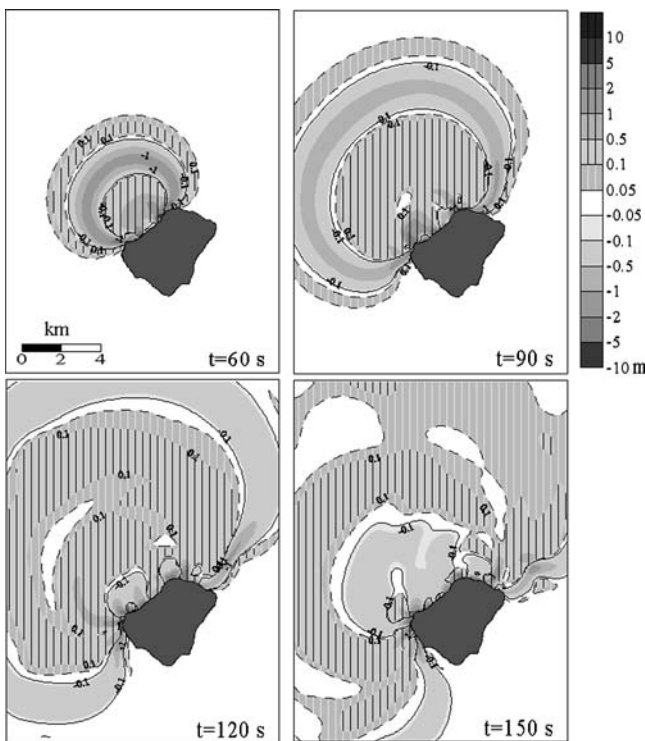

Fig. 7 Submarine-slide tsunami (case 1B). Snapshots of the water elevation fields computed on grid G1. Contour labels are in meters. Palette goes from *white* to *dark grey* as magnitude increases. Positive elevations are *striped*

Fig. 9 Submarine-slide tsunami (case 1B). Computed tide-gauge records. Water elevations are in metres and time in minutes. Notice that each record has its own vertical scale
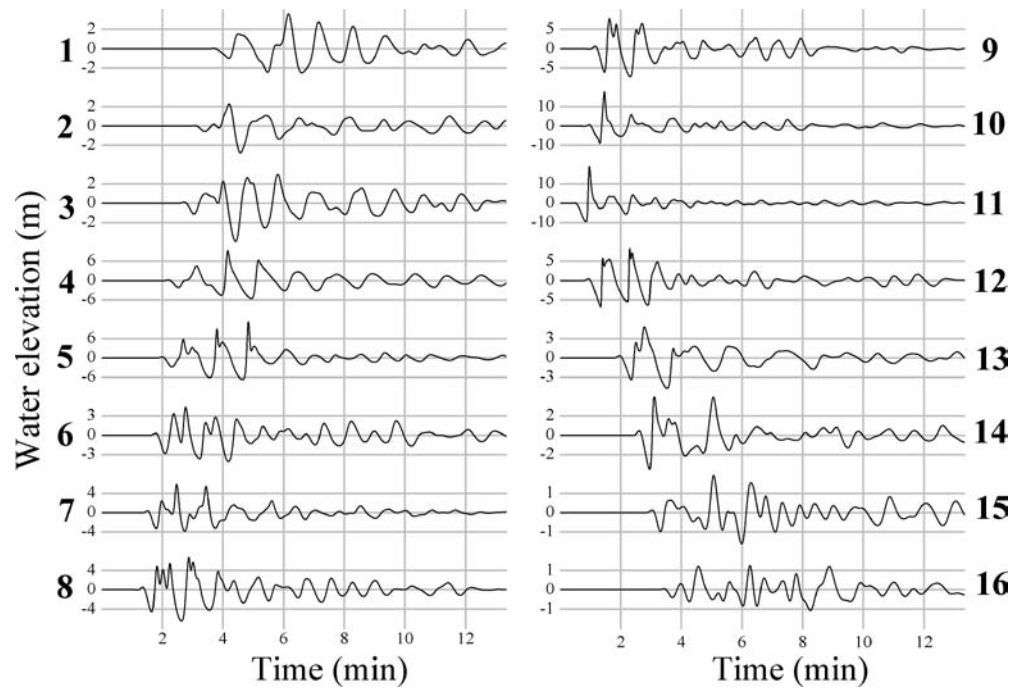
nodes 3 and 4) to Ficogrande (node 5). There are however discrepancies. Most of them are concentrated in the segment between nodes 7 and 8, corresponding to a sequence of small pocket beaches separated by rocky promontories. Here the tsunami impact was influenced strongly by local bathymetry and, more probably, by local inland topography. Therefore, approximating runup heights with the maximum water elevations computed by our model may not be appropriate.

The propagation of the tsunami toward the island of Panarea was computed by means of grid G2. Maps of the water-elevation fields up to 6 min after the tsunami initiation are depicted in Fig. 11. The grid is too coarse to appreciate tsunami details, but propagation fronts and times can be computed correctly. The snapshot taken at 3 min time shows the main offshore fronts that radiate from the source approximately in the form of circular waves. The attack to the Stromboli coast is not yet complete. One min later, the entire coast of Stromboli is already under tsunami attack, while the leading negative wave is about to hit the northern coast of Panarea. In the 5- and 6-min fields, it can be seen that the tsunami has already abandoned the computation domain across three of the boundaries, but it advances slowly southward, since it is slowed down by the shallow waters around the island of Panarea. Two features deserve mention. First, the tsunami propagates towards Panarea as a sequence of waves with wavelengths less than 10 km. Second, tsunami waves tend to remain around Stromboli for a long time. It is a form of energy trapping that occurs when long waves interact with ocean islands; here by long wave we mean a wave with a length comparable with the typical length of the island, a condition that is fulfilled in this case. This propagation feature was already outlined in previous studies on tsunamis (see Tinti and Vannini 1995). It was also predicted to be valid for the specific case of

Stromboli by numerical simulations of tsunamis generated by lateral collapses of the volcanic cone, such as the one that originated the Sciara del Fuoco scar in the Holocene (Tinti et al. 2000, 2003).

The set of Figs. 12–15 serve to illustrate the second tsunami that was caused by the subaerial landslide (case 2). The first water-elevation fields around Stromboli are given in Fig. 12. The mareograms at the set of coastal nodes of Fig. 8 are plotted in Fig. 13. The extreme water elevations at the Stromboli coast are graphed in Fig. 14a and compared to the observed runup values in Fig. 14b (Tinti et al. 2005b), while the tsunami elevation fields computed on grid G2 are shown in Fig. 15. Some of the comments concerning tsunami speed and arrival times, front refraction, and wave trapping hold also for this case. Here it is interesting to stress the main differences. First, this tsunami begins at the coast with a clear water rise, that corresponds to coastal flooding (Fig. 13). The main tsunami signature close to the source seems to be a sequence of crest-trough-crest (see records 10 and 11 of Fig. 13). The extreme values of elevation on the coast (Fig. 14a) decay as the distance from the Sciara del Fuoco source grows, with distribution differing slightly from that of case 1B. Similarities and differences may be better appreciated by examining the zoomed plot of Fig. 14b. This shows that even the computed extremes for case 2 are quite large, but tend to underestimate the observed runup values, though in the area of Ficogrande (node 5) the fit is sufficiently good.

Only the comparison of the extreme sea-level values against the measured runups is presented here for the tsunami simulations of cases 1A and 3. The submarine, a longitudinally uniform and transversally triangular body, whose shape is depicted in Fig. 3 and whose initial position is shown in Fig. 2 (case 1A), produces a tsunami leading to the runups shown in Fig. 16. It can be seen
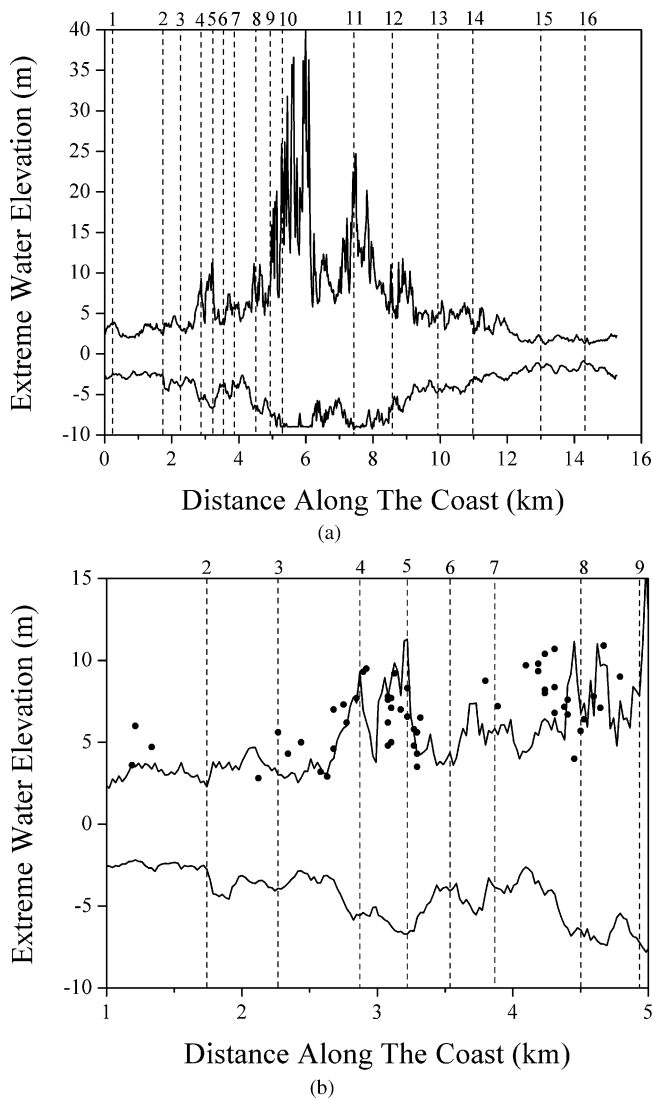
Fig. 10 Submarine-slide tsunami (case 1B). **a** Maximum and minimum water elevation computed along the coastal nodes of grid G1. **b** Detail in the coastal belt where the experimental runup heights (*solid circles*) were measured. The distance is the length of the curvilinear coast taken counterclockwise from a selected origin (*black star* in Fig. 8). *Vertical dotted lines* mark the position on the coast of the nodes given in Fig. 8

that the computed values strongly underestimate the observations. Figure 17 refers to the hypothetical case 3 of a sliding body that has approximately the same size as cases 1A and 1B, but is located partly above and partly below the sea-water level (Fig. 2). The synthetic runups distribution shows a relevant discrepancy with the observations, with a general tendency towards underestimation, with the exception of occasional isolated points where estimates do fit.

Discussion and conclusions

The numerical simulations of the four cases of landslides and tsunamis we have treated here enable us to make some

important remarks. We believe that cases 1B and 2 are the most representative of the 30 December 2002 events, corresponding to the first and to the second main landslide and to the subsequent tsunamis. Cases 1A and 3 have been added in this work to integrate the discussion since they provide interesting elements for the analysis.

The first considerations regard the tsunami generation. The efficiency of the tsunamigenic process is known to be related, among other factors, to the geometry and to the speed of the landslide, and to the water depth. Larger and thicker landslides are believed to produce larger tsunamis. Theoretical analyses using full three-dimensional linear theory of water waves and two-dimensional linear and non-linear shallow-water approximation (Tinti and Bortolucci 2000a; Ward 2001; Liu et al. 2003) as well as analyses of historical cases (Murty 2003), show the positive correlation between tsunami amplitude and landslide thickness and volume. Furthermore, shallow-water approximation predicts that landslides moving underwater at a horizontal speed close to the celerity of long water waves (i.e. $Fr=1$, a condition known as a critical regime), are much more effective in producing tsunamis than slower (subcritical) or very quick (supercritical) landslides (see Tinti and Bortolucci 2000b; Tinti et al. 2001; Trifunac et al. 2002). Moreover, three-dimensional linear analysis shows that landslides in deep oceans generate sea surface perturbations smoother than landslides in shallow oceans, whereas shallow-water theory predicts no difference. This effect of filtering, depending on the depth of the water layer, is taken into account explicitly by our model through the reducing factor $\mathrm{sech}\,\alpha$ that appears in the tsunami excitation term of the hydrodynamics equations.

The shape of the profile of the slide in the direction of motion is another relevant factor. The example of a sliding rigid body can help understand this issue better. In this case, the tsunami excitation term $\partial_t h_s$ depends on the magnitude of the slide thickness gradient along the body trajectory in virtue of the relation $\partial_t H_L = -\vec{V}_h \cdot \nabla H_L$, where $\vec{V}_h$ is the slide horizontal speed. A box-like body has a sudden discontinuous increase (decrease) of thickness at the front (the rear) of the body (since $|\nabla H_L|$ is very large), that imparts a positive (negative) impulse to the sea surface. A typical slide has a smoother profile, but an analogous effect, tending to rise the sea level at the front and to lower it behind. Of course, the effect of the slide impulse on the sea surface is further conditioned by the local depth of the water, due to the depth-dependence of the reducing factor $\mathrm{sech}\,\alpha$.

Slides of cases 1A and 1B are both submarine, and have similar speed, being the slowest of the group (Fig. 4). Their different tsunamigenic power may be yet explained by means of the average transfer function plotted in Fig. 6, but also the different space distribution of this function plays some role, which is worth of clarification. The slide of case 1B has most mass concentrated in the shallow-water region, meaning that its profile is very steep here since it goes from the maximum thickness (about 35 m) to zero over a short distance and is smooth offshore. During the

Fig. 11 Submarine-slide tsunami (case 1B). Snapshots of the water elevation fields computed on grid G2 comprising the sea around the islands of Stromboli and of Panarea. Contour labels are in meters. Palette goes from *white* to *dark grey* as magnitude increases. Positive elevations are *striped*
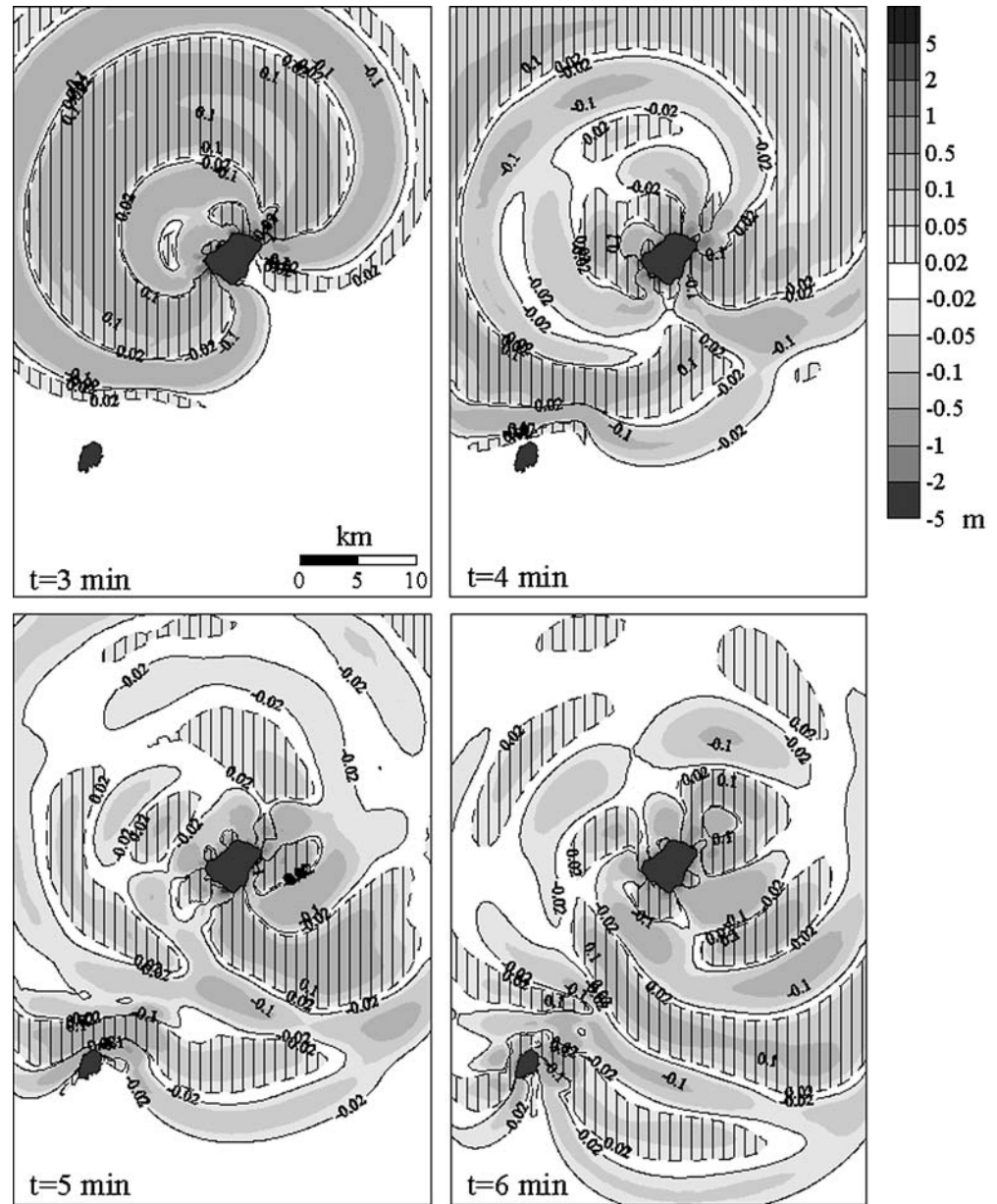

first phase of the motion, this slide imparts big negative impulses in shallow water and small positive impulses in deep water, which are, additionally, more sharply reduced by the depth-dependent filter sech α. Comparatively, the slide of case 1A generates less intense impulses near-shore and larger impulses offshore, but these are cut down by the reducing factor. The net result is that for both slides, the effect of the near-shore negative impulses is prevailing, but these are larger for case 1B than for case 1A, which reflects the relative size of the produced tsunami.

Case 2 is important since it proves that a volume 3–4 times smaller than the volumes involved in the other cases is able to produce a tsunami larger than the tsunami associated with cases 1A and 3 and almost in the same range as the one resulting from the slide of case 1B. This finding can

be explained in virtue of the following considerations. First, this slide is subaerial and gains the largest speed because it starts from a very steep slope (Fig. 4). The slide detaches from above the sea level, and when it enters into the sea completely, it is fast enough to be largely supercritical (Fig. 5). Another relevant aspect is that the corresponding transfer function produces little attenuation in the first 10 s of the motion and is substantially higher than the others up until 25 s (Fig. 6). The combination of the above factors means that the interval of time between 10 and 20 s during which the slide is in a near-critical regime and the filtering effect of the transfer function is large, but not yet dramatic, is the phase of most intense tsunami production. Later, at around 25 s, the slide transits to a subcritical condition crossing again the $Fr=1$ line (see Fig. 5b); this is because

Fig. 12 Subaerial-slide tsunami (case 2). Snapshots of the water elevation fields computed on grid G1. Contour labels are in meters. Palette goes from *white* to *dark grey* as magnitude increases. Positive elevations are *striped*
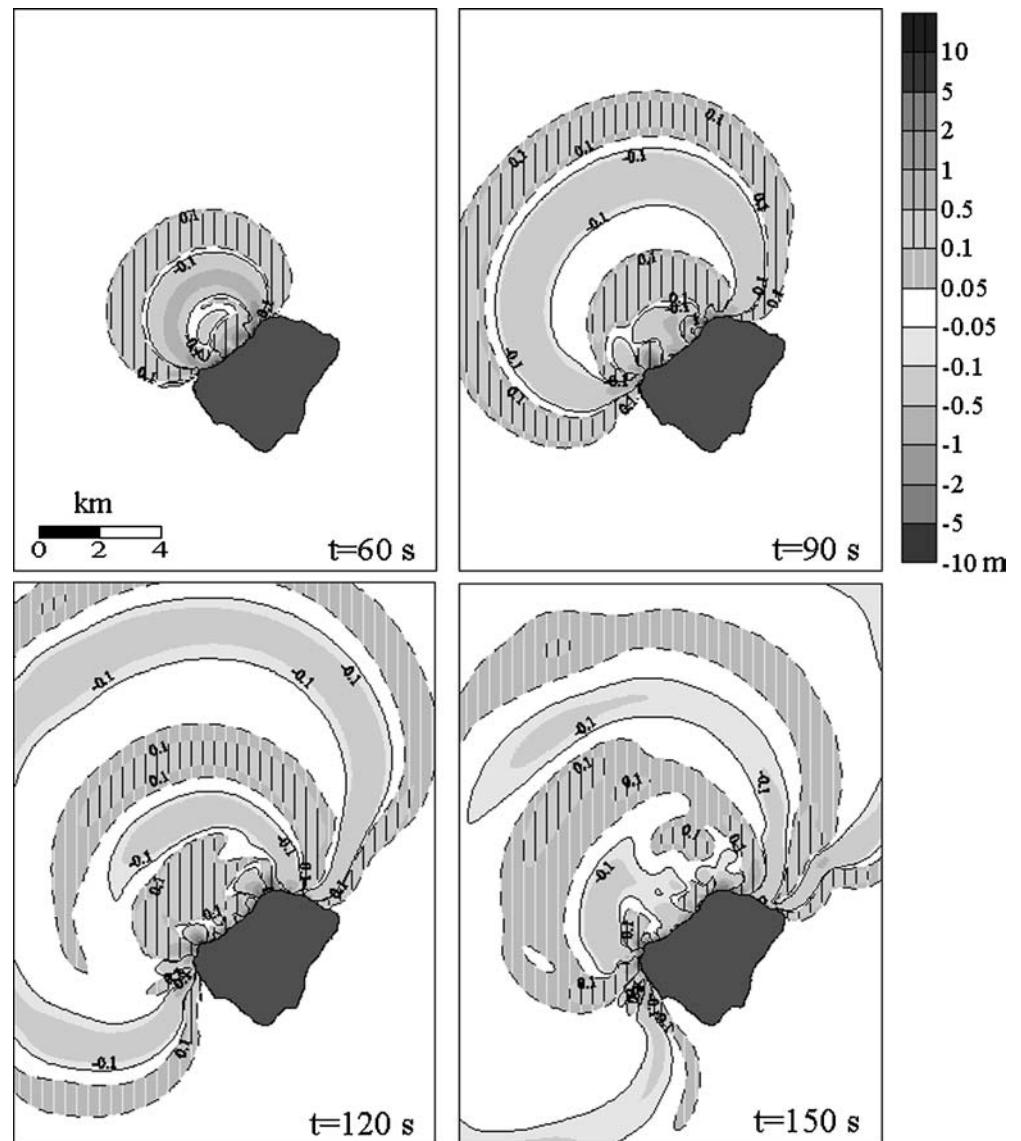

its speed goes down while tsunami celerity goes up, as the slide moves towards larger water depths. However, in this case the attenuation operated by the transfer function is quite effective and, correspondingly, the tsunami excitation term turns out to be quite small.

The criterion based on the Froude number and transfer function graphs is simple and attractive, but cannot catch the full complexity of the generation process, and cannot always be used to estimate the size of the resulting tsunami. An example of such ambiguity comes from the comparison of cases 1A, 1B and case 3. These deal with bodies with the same approximate volumes (16–17 million m³), but with different mass distribution and initial position. The graphs with the extreme water elevations (Figs. 10b, 14b and 17) can be used to rank the resulting tsunami heights. It is seen that case 1B produces the largest tsunami, case 3 is intermediate and case 1A gives the smallest waves that are on average 2–3 times smaller than waves of case 1B. The use of the average Froude numbers and transfer

functions graphed in Figs. 5 and 6 helps explain why the tsunami resulting from case 1A is the weakest; in the first 20–30 s the Froude numbers have similar values, although the transfer function of case 1A is distinctly the smallest. However, it cannot be invoked to clarify the resulting difference (around a factor 1.5–2) between tsunamis of cases 1B and 3. Indeed, both the Froude number and transfer function graphs would point towards favouring the tsunamigenesis of case 3, which is not, however, the case. This proves that the above criterion is rather rough, and cannot replace the use of the simulation code for a correct estimate of the size of the resulting tsunami, whereas it probably turns out to be more valuable for the analysis of cases of idealized water-basin geometries.

The second series of considerations concerns tsunami propagation. The results of our simulations must be compared with the observations that are the accounts of the eyewitnesses (Tinti et al. 2005a) and the findings of the post-event field surveys (Tinti et al. 2005b). Only a few

Fig. 13 Subaerial-slide tsunami (case 2). Computed tide-gauge records. Water elevations are in metres and time in minutes. Notice that each record has its own vertical scale
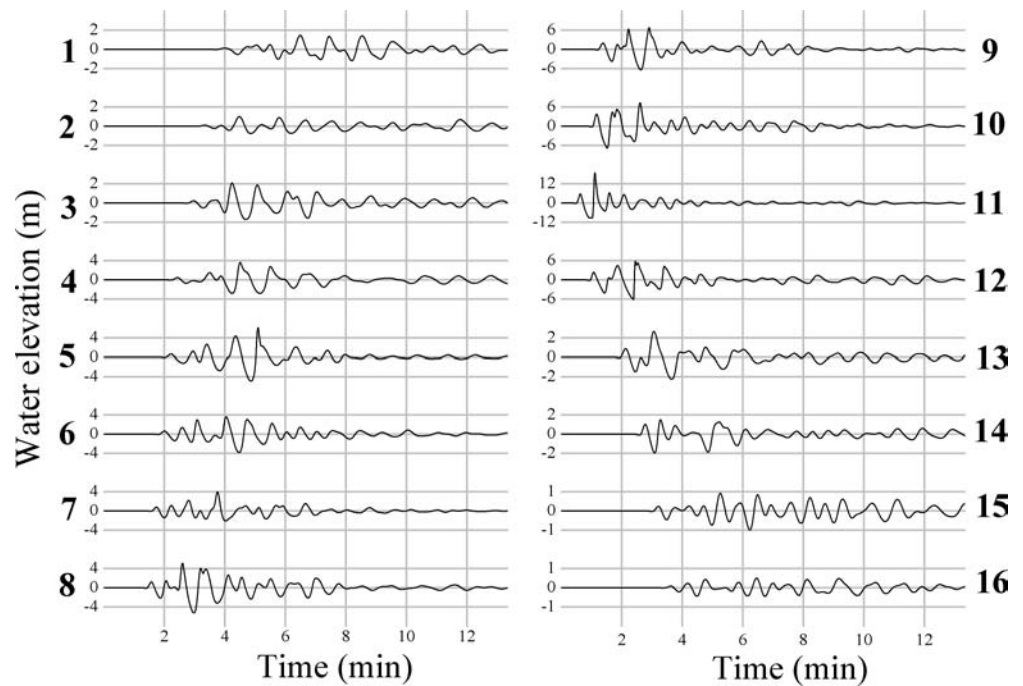
people were able to distinguish the arrival of two tsunamis, probably because the 7-min time separation between the two events was too short, and the second arrival was superposed to the queue of the first. However, those who had observed the events since the beginning agree that they saw a water withdrawal first. This is well explained by our simulations. In fact, the first tsunami, represented by the case 1B, has a small positive leading wave (see water elevation fields of Fig. 7), but in the tide-gauge records computed at the coastal nodes of Stromboli (Fig. 9), this positive wave either does not exist or is very minor and practically undetectable by people whose attention was attracted by the following substantial retreat of the sea. On the other hand, the tsunami of case 2, that is the second tsunami in our mind, has a well-defined positive first arrival.

The number of large waves differs from place to place and is related both to the bathymetry and to the source. First, the signal tends to be simpler in the nodes close to the Sciara-del-Fuoco region where the signature of the source is quite evident: a dipole trough-crest sequence for the first tsunami, a triple crest-trough-crest for the second. In more distant nodes, the sequence of the main oscillations becomes longer and more complex. In some nodes both simulations (cases 1B and 2) give the same number of large waves, which means that the effect of local bathymetry is predominant. For example, this occurs for node 5 corresponding to Ficogrande (see computed mareograms in Figs. 9 and 13). Here an eyewitness reported to have seen both tsunamis and to have observed a sequence of waves for both of them. A further remark is about the relative wave amplitude. The first wave is not always the largest one. In several cases the largest wave is the second or the third of the wave train. The computed waveforms in the mareograms are not symmetrical: the water rise is faster than the water fall, which suggests that the shape of the

wave is also asymmetrical with a steep transition from the trough to the crest of the wave. An observer inland would see the wave approaching the coast like an almost vertical wall of water. Probably these waves are prone to break, and wave breaking was seen and documented by some eyewitnesses to occur very close to the coast in some places. Wave breaking is not included in the model, which, however, accounts for energy dissipation as the waves interact with the coastal boundaries.

An important aspect is the direction of the tsunami fronts that is dominated by the bathymetry. Refraction causes bending of the fronts that travel around the island of Stromboli, hitting the coast obliquely. This was observed by many people, and was also documented by the post-tsunami surveys, since currents associated with the attacking waves left visible marks of their direction; in particular, the flooding water had enough momentum to bend the iron posts of several wire nettings and fences downstream.

The most important dataset collected by the post-event surveys is the set of the runup heights. After the events, there was no way to discriminate between the heights of the first and the second tsunami. What was seen was the cumulative effect. The observers did not clarify completely which one was larger. From some accounts we know that the first tsunami was destructive in some places such as in Ficogrande (node 5 in Fig. 8). From others, we know that the second tsunami attacked the northern Punta Lena (between nodes 3 and 4) with great violence. From a further report we know that both tsunamis caused similar flooding in Scari (node 3). Our simulations show that both landslides, the submarine of case 1B and the subaerial of case 2, are able to produce destructive waves on the northeastern coast of Stromboli. The extreme water elevation compared to the runup heights (Figs. 10b and 14b) give satisfactory
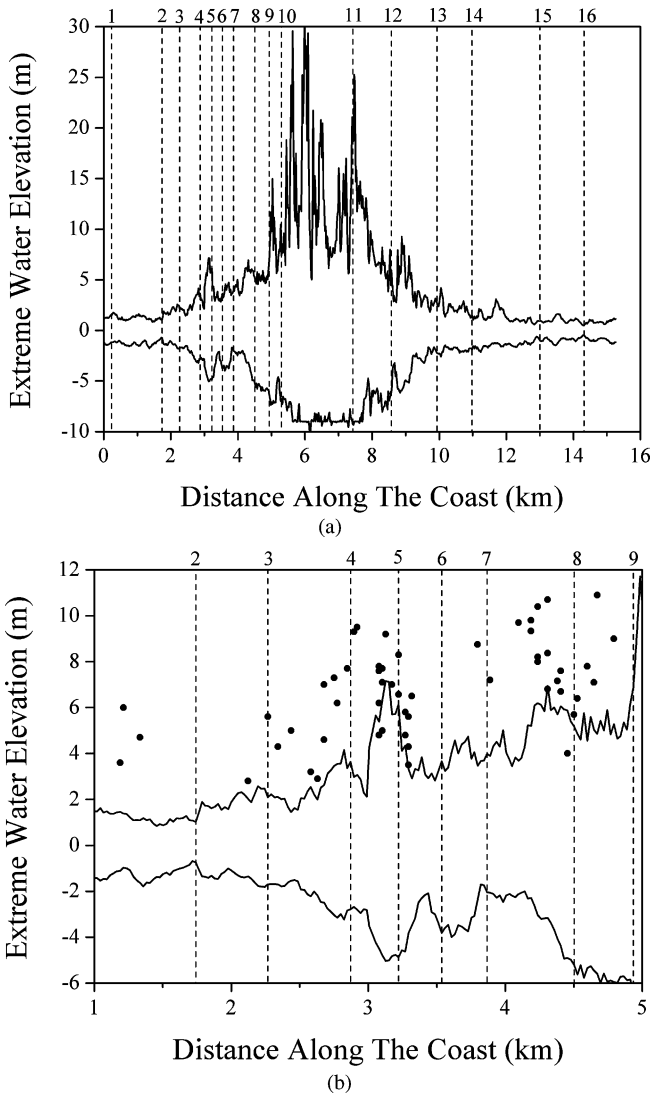
Fig. 14 Subaerial-slide tsunami (case 2). **a** Maximum and minimum water elevation computed along the coastal nodes of grid G1. **b** Detail in the coastal belt where the experimental runup heights (*solid circles*) were measured. See caption of Fig. 10 for the rest

Fig. 15 Subaerial-slide tsunami (case 2). Snapshots of the water elevation fields computed on grid G2

Fig. 16 Submarine-slide tsunami (case 1A). Extreme water elevation computed along the coastal nodes of grid G1 in the region where runup heights were measured (*solid circles*). See caption of Fig. 10b for the rest

results, showing, however, that the first tsunami was generally larger than the second.

The final observation regards the propagation time. The tsunamis were quite slow around Stromboli, though they were quick enough to hit the entire coast of the island in less than 4 min. As expected, they were faster in deep water, and they arrived at the island of Panarea in little less than 5 min. This has been estimated by means of the simulations performed over the coarse grid G2 and is shown in Figs. 11 and 15. This propagation time can be checked in the records of three broadband seismometer stations of a mobile network that were installed on the island of Panarea at a short distance from the coast and that recorded both the signal of the landslides and the impact of the tsunamis (La Rocca et al. 2004). The agreement is very satisfactory.
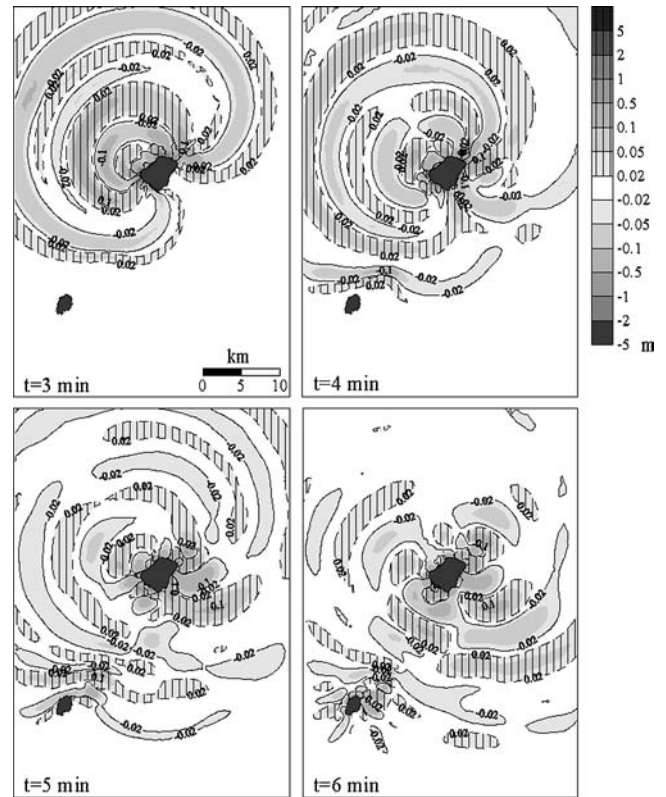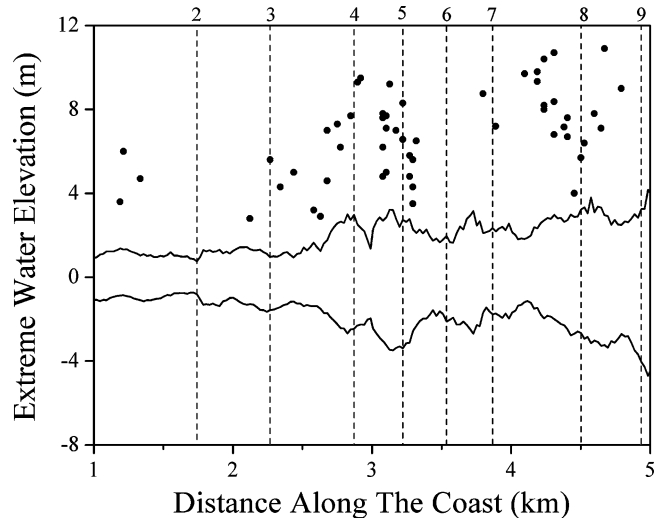
In conclusion, it can be stated that the numerical simulations of the landslide-induced tsunamis provide a good explanation of the facts. The model can be certainly improved, for example by extending the grid to cover the inland topography and by accounting for explicit computations of flooding, but we do not think that enhancement of the numerical code could lead to substantially
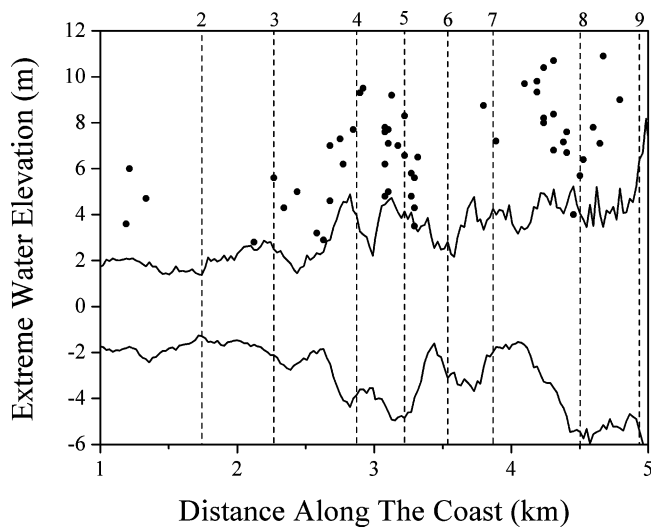
Fig. 17 Submarine-subaerial-slide tsunami (case 3). See caption of Fig. 10b

more reliable results in the absence of better knowledge of the source, that is of the landslides that generated the tsunamis.

References

Baldi P, Belloli F, Fabris M, Marsella M, Ponticelli R, Signorotto V (2003) La fotogrammetria digitale differenziale del versante della Sciara del Fuoco (isola di Stromboli) dopo l'evento del 30 Dicembre 2002 (in Italian). 7ᵃ Conferenza Nazionale ASITA "L'informazione territoriale e la dimensione del tempo", Verona 28–31 Ottobre 2003

Bonaccorso A, Calvari S, Garfì G, Lodato L, Patané D (2003) Dynamics of the December 2002 flank failure and tsunami at Stromboli volcano inferred by volcanological and geophysical observations. Geophys Res Lett 30(18):1941 DOI10.1029/2003GL017702

Bortolucci E (2001) Modelli dinamici di frane e dei maremoti indotti. PhD Thesis, Dottorato di Ricerca in Fisica, XIV Ciclo, a.a. 2000–2001, Università di Bologna, Bologna, pp 1–126

Chen H, Lee CF (2003) A dynamic model for rainfall-induced landslides on natural slopes. Geomorph 51:269–288

Chiocci FL, Bosman A, Romagnoli C, Tommasi P, De Alteris G (2003) The December 2002 Sciara del Fuoco (Stromboli Island) submarine landslide: a first characterisation. EGS-AGU-EUG Joint Assembly, Nice, France, April 2003, Geophysical Research Abstracts, vol.5, CDROM Version

Choi BH, Pelinovsky E, Hong SJ, Woo SB (2003) Computation of tsunamis in the East (Japan) Sea using dynamically interfaced nested model. Pure Appl Geophys 160:1383–1414

Dattilo G, Spezzano G (2003) Simulation of a cellular landslide model with CAMELOT on high performance computers. Parallel Comput 29:1403–1418

Gusiakov VK (2001) "Red", "Green" and "Blue" tsunamigenic earthquakes and their relation with conditions of oceanic sedimentation in the Pacific. In: Hebenstreit GT (ed) Tsunami research at the end of a critical decade, Advances in natural and technological research, vol. 18. Kluwer, Dordrecht, pp 17–32

Harbitz CB (1992) Model simulations of tsunamis generated by the Storegga slides. Mar Geol 105:1–21

Hebert H, Piatanesi A, Heinrich P, Schindele F, Okal EA (2002) Numerical modeling of the September 13, 1999 landslide and tsunami on Fatu Hiva Island (French Polynesia). Geophys Res Lett 29(10):1484 DOI10.1029/2001GL013774

Jiang L, LeBlond PH (1992) The coupling of a submarine slide and the surface waves it generates. J Geophys Res 97:12731–12744

Jiang L, LeBlond PH (1994) Three-dimensional modeling of tsunami generation due to a submarine mudslide. J Phys Oceanogr 24:559–572

La Rocca M Galluzzo D, Saccorotti G, Tinti S, Cimini G, Del Pezzo E (2004) Seismic signals associated with landslides and with a tsunami at Stromboli volcano, Italy. Bull Seis Soc Am 94:1850–1867

Liu PL-F, Lynett P, Synolakis CE (2003) Analytical solutions for forced long waves on a sloping beach. J Fluid Mech 478:101–109

Louge MY, Keast SC (2001) On dense granular flows down flat frictional inclines. Phys Fluids 13:1213–1233

Kajiura K (1963) The leading wave of a tsunami. Bull Earthquake Res Int 41:535–571

Kidd RB, Lucchi RG, Gee M, Woodside JM (1998) Sedimentary processes in the Stromboli canyon and Marsili Basin, SE Tyrrhenian sea: results from side-scan sonar surveys. Geo Mar Lett 18:146–154

Mader CL (1988) Numerical modeling of water waves. Univeristy of California Press, Berkeley, pp 1–206

Maramai A, Graziani L, Tinti S (2005) Tsunami in the Aeolian islands (southern Italy): a review. Mar Geol 215:11–21

Murty TS (2003) Tsunami wave height dependence on landslide volume. Pure Appl Geophys 160:2147–2153

Pino NA, Ripepe M, Cimini GB (2004) The Stromboli volcano landslides of December 2002: a seismological description. Geophys Res Lett 31:L02605 DOI10.1029/2003GL0118385

Pitman EB, Nichita CC, Patra AK, Bauer AC, Bursik M, Webb A (2003) A model of a granular flow over an erodable surface. Discrete Cont Dynam Sys Ser B, 3:589–599

Rabinovich AB, Thomson RE, Bornhold BD, Fine IV, Kulikov EA (2003) Numerical modelling of tsunamis generated by hypothetical landslides in the Strait of Georgia, British Columbia. Pure Appl Geophys 160:1273–1313

Satake K (1995) Linear and nonlinear computations of the 1992 Nicaragua earthquake tsunami. Pure Appl Geophys 144:455–470

Scherreiks R (2000) A note on turbidites and debrites in the vicinity of the Aeolian Islands, SE Tyrrhenian Sea. Geo Mar Lett 20:58–61

Tinti S, Vannini C (1995) Tsunami trapping near circular islands. Pure Appl Geophys 144:595–619

Tinti S, Bortolucci E, Vannini C (1997) A block-based theoretical model suited to gravitational sliding. Nat Hazards 16:1–28

Tinti S, Bortolucci E, Armigliato A (1999) Numerical simulation of the landslide-induced tsunami of 1988 in Vulcano island, Italy. Bull Volcanol 61:121–137

Tinti S, Bortolucci E (2000a) Analytical investigation on tsunamis generated by submarine slides. Annal Geofis 43:519–536

Tinti S, Bortolucci E (2000b) Energy of water waves induced by submarine landslides. Pure Appl Geophys 157:281–318

Tinti S, Bortolucci E, Romagnoli C (2000) Computer simulations of tsunamis due to flank collapse at Stromboli, Italy. J Volcanol Geoth Res 96:103–128

Tinti S, Bortolucci E, Chiavettieri C (2001) Tsunami excitation by submarine slides in shallow-water approximation. Pure Appl Geophys 158:759–797

Tinti S, Pagnoni G, Zaniboni F, Bortolucci E (2003) Tsunami generation in Stromboli and impact on the south-east Tyrrhenian coasts. Nat Hazards Earth Sys Sci 3:299–309

Tinti S, Maramai A, Graziani L (2004) The new catalogue of Italian tsunamis. Nat Haz 33:439–465

Tinti S, Manucci A, Pagnoni G, Armigliato A, Zaniboni F (2005a) The 30th December 2002 tsunami in Stromboli: sequence of the events reconstructed from the eyewitness accounts. Nat Hazards Earth Sys Sci (5: 763–775)

Tinti S, Maramai A, Armigliato A, Graziani L, Manucci A, Pagnoni G, Zaniboni F (2005b) Quantitative observations of the physical effects of the Stromboli tsunamis occurred on December 30, 2002. Bull Volcanol (this issue) (in press)

Trifunac MD, Hayir A, Todorovska MI (2002) A note on the effects of nonuniform spreading velocity of submarine slumps and slides on the near-field tsunami amplitudes. Soil Dyn Earthquake Eng 22:167–180

Ward SN (2001) Landslide tsunami. J Geophys Res 106 (B6):11:201–216 .

Ward SN, Day S (2002) Suboceanic landslides. In: 2002 yearbook of science and technology. McGraw-Hill, New York, pp 349–352

Ward SN, Day S (2003) Ritter island volcano: lateral collapse and the tsunami of 1888, Geophys J Int 154:891–902

Watts P (2000) Tsunami features of a solid block underwater landslides. J Waterways Port Coast Ocean Eng ASCE 126:144–152

Zaniboni F (2004) Modelli numerici di evoluzione di frane con applicazione a casi di frane tsunamigeniche subaeree e sottomarine. PhD Thesis, Dottorato di Ricerca in Modellistica Fisica per la Protezione dell'Ambiente, XVI Ciclo, a.a. 2003–2004, Università di Bologna, Bologna, pp 1–112